Effect of substrate heterogeneity and topology on epithelial tissue growth dynamics

Mahmood Mazarei,[1,*] Jan Åström,[2,†] Jan Westerholm,[3,‡] and Mikko Karttunen[1,4,§]

[1]*Department of Physics and Astronomy, Western University, 1151 Richmond Street, London, Ontario, Canada N6A 3K7*

[2]*CSC Scientific Computing Ltd, Kägelstranden 14, 02150 Esbo, Finland*

[3]*Faculty of Science and Engineering, Åbo Akademi University, Vattenborgsvägen 3, FI-20500 Åbo, Finland*

[4]*Department of Chemistry, Western University, 1151 Richmond Street, London, Ontario, Canada N6A 5B7*

(Received 20 March 2023; revised 6 July 2023; accepted 20 September 2023; published 13 November 2023)

Tissue growth kinetics and interface dynamics depend on the properties of the tissue environment and cell-cell interactions. In cellular environments, substrate heterogeneity and geometry arise from a variety factors, such as the structure of the extracellular matrix and nutrient concentration. We used the CELLSIM3D model, a kinetic cell division simulator, to investigate the growth kinetics and interface roughness dynamics of epithelial tissue growth on heterogeneous substrates with varying topologies. The results show that the presence of quenched disorder has a clear effect on the colony morphology and the roughness scaling of the interface in the moving interface regime. In a medium with quenched disorder, the tissue interface has a smaller interface roughness exponent, α, and a larger growth exponent, β. The scaling exponents also depend on the topology of the substrate and cannot be categorized by well-known universality classes.

DOI: 10.1103/PhysRevE.108.054405

I. INTRODUCTION

Understanding the role of mechanobiological phenomena in complex biological processes such as wound healing, tumor growth, and morphogenesis necessitates the study of the physical interactions between cells and their environments. *In vivo*, heterogeneities of different types are always present and they play an important role in regulating tumor invasion [1,2]. One of the prime examples is the extracellular matrix, which typically provides support for cells and is a key factor for cell adhesion and the differentiation of cells [3,4]. Heterogeneities can also be produced by the addition of pharmacological agents or (gelly) materials, such as methylcellulose, or by changing the nutrient concentration, as well as by other means [5–7]. The presence of heterogeneities, or disorder in physical terms, often influences biochemical and biomechanical parameters, such as cell-cell interactions, the rate of cell division, and the average cell size and shape, and thus alters cell mobility, colony spreading, and the roughness of the colony interface [5,6]. In addition, the situation can be even more complex, such as in the epithelial-to-mesenchymal and mesenchymal-to-epithelial transitions during which the whole cellular environment undergoes fundamental and complex changes [8].

Tumor growth, and therapy to prevent it, may be characterized as cellular processes involving molecular inter- and intracellular control [9]. Studying the roughness of tumor surfaces is necessary for the development of diagnostic and therapeutic methods [10]. Recent studies have, for example, indicated that tumor surface regularity is a significant predictor of glioblastoma patients' chances of survival [11,12]. Mathematical and computer models are increasingly being used to examine and measure the influence of different biophysical parameters on biological processes such as nonequilibrium pattern generation in biological growth [6,13–16]. In our previous study, we demonstrated that the mechanical properties of cells can have a significant impact on the surface roughness dynamics of cell colonies [17]. The current paper focuses on the growth on heterogeneous substrates.

The spreading of a cellular colony, e.g., tumor, healthy, or bacterial, can be seen as the propagation of an elastic interface in the presence of a pinning potential that arises from the surrounding environment. Analogous phenomena occur in diverse systems including vortex motion in type-II superconductors [18], charge-density waves [19,20], and fracture propagation [21]. For such systems, one typically distinguishes between strong and weak pinning. In the former case, the pinning energy (per impurity) is much larger than the elastic energy leading to local energy minimization, while in the weak pinning regime, the opposite is true and the interface adjusts collectively.

When the interface has adjusted to the disorder and is not moving, it is in the pinned phase. When a driving force is applied and it exceeds a threshold force, F_c, the interface undergoes a depinning transition and enters the moving phase. The size of the advancing regions is then characterized by a correlation length (ξ) which diverges upon approaching the critical force from above, $\xi = (F - F_c)^{-\nu}$, where ν denotes the correlation length exponent [22]. It is also common to differentiate between annealed and quenched disorder. In the latter, disorder is considered as stationary, that is, the motions

*mmazare@uwo.ca
†jan.astrom@csc.fi
‡jan.westerholm@abo.fi
§mkarttu@uwo.ca

of the pinning sites are much slower than any other relevant timescale in the system; in the annealed case, this assumption no longer holds. In this paper, only quenched disorder is considered. In addition, since here the driving force enters through cell division, we are not interested in the depinning transition itself.

Studying the roughness of tumor surfaces is useful for distinguishing the dominant growth mechanisms, such as surface diffusion and lateral growth that influence the growth, morphology, and progression of tumors. Dynamic scaling analysis provides powerful tools to classify growth. Dynamic critical exponents, namely, the roughness (α), growth (β), and dynamic exponent (z) can be determined from the time evolution of the front's roughness; the cell colony's front in this case [10,16,23–29]. In addition to the above, the dynamic exponent is related to the two other exponents via $z = \frac{\alpha}{\beta}$.

Several dynamic universality classes have been proposed for interface growth. The Kardar-Parisi-Zhang (KPZ) dynamic universality class [30] describes the evolution of a surface using a continuous nonlinear stochastic differential equation

$$\partial_t h(x,t) = -\lambda[\partial_x h(x,t)]^2 + \nu\partial_x^2 h(x,t) + \eta(x,t), \quad (1)$$

where $h(x,t)$, the height, is the distance from the ith point at the colony front to the baseline of the colony. Lateral growth normal to the interface, reflected in the quadratic term $-\lambda(\partial_x h)^2$, is a characteristic of the KPZ universality class. Surface tension is accounted for by the Laplacian term, $\nu\partial_x^2 h$, which tends to flatten the surface, and $\eta(x,t)$ is an uncorrelated Gaussian noise given by $\langle\eta(x,t)\rangle = 0$ and $\langle\eta(x,t)\eta(x',t')\rangle = 2D\delta(x-x')\delta(t-t')$.

In the quenched KPZ (qKPZ) equation, the thermal noise in Eq. (1) is replaced by a position-dependent noise, that is, $\eta(x,t)$ becomes $\eta(x,h)$ with $\langle\eta(x,h)\rangle = 0$ and $\langle\eta(x,h)\eta(x',h')\rangle = 2D\delta(x-x')\delta(h-h')$. Since thermal noise is usually present in experiments, the qKPZ equation can be extended to contain both quenched and thermal noise.

Distinct critical exponents and universality classes are described by different growth equations. For KPZ, the critical exponents are $\alpha^{\mathrm{KPZ}} = \frac{1}{2}$, $\beta^{\mathrm{KPZ}} = \frac{1}{3}$, and $z^{\mathrm{KPZ}} = \frac{3}{2}$ for one-dimensional interfaces [30]. For the quenched KPZ equation, dynamic critical exponents haven been determined to be $\alpha^{\mathrm{qKPZ}} = \frac{3}{4}$, $\beta^{\mathrm{qKPZ}} = \frac{3}{5}$, and $z^{\mathrm{qKPZ}} = \frac{5}{4}$ [31]. The critical exponents of the linear molecular beam epitaxy (MBE) equation for a one-dimensional interface are $\alpha^{\mathrm{MBE}} = \frac{3}{2}$, $\beta^{\mathrm{MBE}} = \frac{3}{8}$, and $z^{\mathrm{MBE}} = 4.0$.

In one-dimensional quasilinear and quasicircular expanding interfaces, previous experimental research on cells grown on culture without quenched disorder have presented various scaling behaviors [10,26,28,29,32]. Brú *et al.* [10,26] suggested that the development dynamics of both malignant and normal cell colonies are characterized by the exponents $\alpha = 1.5 \pm 0.15$, $\beta = 0.38 \pm 0.07$, and $z = 4 \pm 0.5$ that belong to the MBE universality class. This was reported for both *in vitro* and *in vivo* experiments. In contrast, however, Huergo *et al.* reported the exponents $\alpha = 0.50 \pm 0.05$, $\beta = 0.32 \pm 0.04$, and $z = 1.56 \pm 0.1$ for interfacial growth of HeLa (cervix cancer) cell colonies *in vitro* [28,29,32]. Plant calli, *Brassica oleracea* and *Brassica rapa*, were studied by Galeano *et al.*, who reported exponents inconsistent with both MBE and KPZ, $\alpha = 0.86 \pm 0.04$ and $z = 5.0$ [7].

Biological systems with substrate disorder appear in situations such as growing bacterial colonies on agar-containing media and in the development of bacterial biofilms. In *Escherichia coli* and *Bacillus subtilis* colonies, Vicsek *et al.* [33] found the roughness exponent $\alpha = 0.78 \pm 0.07$, which exceeds the KPZ value. Huergo *et al.* reported qKPZ-compatible exponents $\alpha = 0.63 \pm 0.04$, $\beta = 0.75 \pm 0.05$, and $z = 0.84 \pm 0.05$ for the development of quasilinear Vero cell colony fronts in culture media containing methylcellulose [5]. Santalla *et al.* conducted experiments at high agar concentrations and found branching interfaces whose scaling exponents were in complete disagreement with both the KPZ and qKPZ scaling exponents [34]. Rapin *et al.* studied the effects of pharmacological agents on the geometry and roughness dynamics of *in vitro* propagating Rat1 fibroblast cell interfaces and reported two separate scaling regimes, the first at the subcell level and the second at intermediate length scales of 2–10 cells [6].

Various theoretical and computational models have been developed to examine surface growth with quenched disorder. The directed percolation depinning model predicts α to be between 0.66 and 0.73, and $\beta = 0.68 \pm 0.04$ [35]. Models of self-organized growth have predicted $\beta = 0.9 \pm 0.1$ and $\alpha = 0.63 \pm 0.02$ [36], and a numerical study of an automaton model yielded $\alpha = 0.63 \pm 0.01$ and $\beta = 0.64 \pm 0.02$ [37]. Santalla and Ferreira incorporated nutrient diffusion to an off-lattice Eden model and reported a transition from a transient KPZ-like regime with $\beta = 0.34 \pm 0.01$ to an unstable growth regime with $\beta = 0.43 \pm 0.02$, with an intermediate transient regime belonging to the qKPZ universality class with $\beta = 0.633$ and local roughness exponents ranging within $0.39 < \alpha_{\mathrm{loc}} < 0.67$ [38].

Further computational and theoretical studies have demonstrated the effects of cell-cell mechanical tensions and nutrient concentration and distribution on the spatial structures with morphologies ranging from smooth to heavily fingered interfaces [39,40]. Simulations of two-dimensional cellular colonies by Block *et al.* showed KPZ-like dynamics for a class of cellular automata models over a broad range of parameters [41]. Azimzade *et al.* used the Fisher-Kolmogorov-Petrovsky-Piskunov (FKPP) equation to study the effect of the cellular environment's stiffness and spatial correlations on the morphology of the interface of growing tumors, and concluded that the KPZ equation cannot describe their tumor development model [42]. Bonachela *et al.* developed an off-lattice cell model with quenched disorder describing competition among bacterial cells for space and resources. They reported the exponents $\alpha = 0.68 \pm 0.05$, $\beta = 0.61 \pm 0.05$, and $z = 1.11 \pm 17$ for the moving regime [43]. Pinto *et al.* modified the self-propelled Voronoi model of Bi *et al.* [44] to study the effect of spatial disorder of the cell-substrate interaction, defined as having stiff cells in the tissue, on cell motility in a confluent tissue, reporting $\beta = 0.194 \pm 007$ [45]. In our previous work, we showed that a cell colony can show both KPZ- and MBE-like scaling dynamics depending on the strength of the cell-cell adhesion between the cells and the cell colony's geometry [17].

II. METHODS

A. CellSim3D simulator and model

CellSim3D is a coarse-grained molecular dynamics-based model of cellular dynamics with an emphasis on mechanobiological features of tissue growth [46]. The code is open source [47]. CellSim3D allows cellular growth to be modeled in two (epithelial growth) or three dimensions, and cells are modeled as three-dimensional objects consisting of a set of interconnected nodes. Here, the geometry and the nodes are those of a spherical C180 fullerene. A detailed description of the model is provided in the Supplemental Material [48]. Below we provide a brief description of it.

The CellSim3D force field consists of intra- and intercellular forces and a noise term (η):

$$m\ddot{\mathbf{r}} = \mathbf{F}^{\mathrm{B}} + \mathbf{F}^{\theta} + \mathbf{F}^{\mathrm{R}} + \mathbf{F}^{\mathrm{A}} + \mathbf{F}^{\mathrm{F,e}} + \mathbf{F}^{\mathrm{F,m}} + \mathbf{F}^{\mathrm{P}} + \eta. \quad (2)$$

The two intracellular forces on the surfaces of the cells are $\mathbf{F}^{\mathrm{B}}$, a damped harmonic oscillator force between the nearest-neighboring nodes with a spring constant (k^{B}) and a friction coefficient (γ_{int}), and $\mathbf{F}^{\theta}$, the angle force which is a harmonic potential depending on the equilibrium angles between the nodes with a spring constant (k^{θ}). The angle term preserves the cell's surface curvature. For simplicity, the spring constants for both the angle force and the damped spring force between the nodes are assumed to be constant over the cell surface.

Intercellular forces in CellSim3D consist of both cell-cell and cell-environment interactions. In biological cells, the cell-cell interactions are mainly caused by cell adhesion molecules (CAMs) [49–51]. Here, the intercellular forces are described by a repulsive force, $\mathbf{F}^{\mathrm{R}}$, and an attractive force, $\mathbf{F}^{\mathrm{A}}$, between two nodes in neighboring cells. In addition, the model also includes a friction force, $\mathbf{F}^{\mathrm{F}}$, between two cells that pass by each other. The repulsive and attractive forces between the cells are represented, respectively, by short-range harmonic potentials with distinct cutoffs R_0^{R}, R_0^{A}, and spring constants k^{R}, k^{A}. In this paper, we assume that the adhesion molecules are distributed uniformly across the cell surface, and that the adhesion and repulsion spring constants (k^{A}, k^{R}) are identical for all nodes on the surface. The intermembrane friction force, $\mathbf{F}^{\mathrm{F,e}} = -\gamma_{\mathrm{ext}}\,\mathbf{v}_{ij}^{\tau_{\mathrm{m}}}$, is defined up to a cutoff range, R_0^{A}, between the nodes i and j on two separate cells as a function of the tangential relative velocity to the cell surfaces, $\mathbf{v}_{ij}^{\tau_{\mathrm{m}}}$. The intermembrane friction coefficient, γ_{ext}, is assumed to be constant across the cells.

The friction force, $\mathbf{F}^{\mathrm{F,m}} = -\gamma_{\mathrm{m}}\,\mathbf{v}$, approximates the interactions between the cell and its environment, and it is defined as a viscous drag force from a fluid medium. The growth force, $\mathbf{F}^{\mathrm{P}} = PS\hat{\mathbf{n}}$, is determined by the cell's internal pressure resulting from the osmotic pressure within the cell [49], where $\hat{\mathbf{n}}$ is an outward pointing normal to the surface of the cell and PS is the force due to a growing pressure inside the cell. This growing force compensates for the cell membrane elasticity modeled by harmonic potentials. Finally, the noise term, η, is defined as a Gaussian white noise with $\langle\eta(x,t)\rangle = 0$ and $\langle\eta(x,t)\eta(x',t')\rangle = 2D\delta(t-t')\delta(x-x')$.

At each time step, the internal pressure increases by the growth rate $\Delta(PS)$, resulting in a gradual increase in the pressure force ($\mathbf{F}^{\mathrm{P}}$) and the cell volume. However, the repulsive forces from the neighboring cells oppose the internal pressure force of the cell. This competition determines whether a cell will continue to grow or cease growing. This was characterized in detail in our previous work [52], and the findings agree very well with experiments [53]. At confluence and in dense regions, the colony rearranges itself (see the denser interior areas in the videos provided as Supplemental Material [48]). The rate at which cells can move and the colony to rearrange itself depends on a number of variables, including the magnitude of the random force, the viscosity of the medium, and the forces exerted by neighboring cells [52]. The effect of density and crowding on the growth rate has been studied previously by Madhikar *et al.* [54]. The results, in particular the size distributions, are in excellent agreement with experimental results of the *Drosophila* wing disk growth [55].

When the volume of the cell reaches a critical threshold, given by the parameter V_{div}, the cell divides into two daughter cells. The distinguishing characteristics of the cell division are the orientation and the location of the division plane. Cell division can be either symmetric or asymmetric, depending on the position of the division plane. In this paper, we used symmetric cell division, in which the volumes of the daughter cells become half the volume of the parent cell, and the mechanical properties are a copy of the parent cell's properties. The division algorithm accounts for the planar expansion of epithelial tissue: The division plane is selected by randomly sampling a vector from a circle in the plane defined by the vector normal to the epithelial plane. To prevent buckling during epithelial growth, three-dimensional cells are confined between two frictionless plates with repulsion in the direction normal to the plates [17,54]. More details of the theoretical basis, the code implementation, and the mapping of the parameters can be found in Refs. [17,46,54]. Parameters for the simulations performed in this paper are provided in Table I.

B. Disorder

Pinning impurities were randomly positioned (at time $t = 0$) as immobile cells that do not grow. They interact with regular cells via adhesion, repulsion, and friction, with the same strengths as regular cells do. Cells can squeeze and move between two immobile cells. This is well demonstrated in the videos provided as Supplemental Material [48]; the two videos of systems with disorder have the text `with_disorder` in their names and the pinning centers are shown in black. Importantly, when the adhesion interaction between the cells is strong, so is the interaction between the cells and the disorder. The same applies for the case of weak cell-cell interaction. The pinned cells maintain their spherical shapes and sizes throughout the simulation. For each simulated parameter set, ten independent simulations for an extended period of time up to the order of $O(10^5)$ cells were performed for data averaging. Table S1 demonstrates that the minimum required sample size with a margin of error of 0.1 is of the order of 10; the discussion in Supplemental Material [48] provides estimates for the minimal sample sizes. The parameters for quenched disorder are shown in Table II.

C. Colony configurations

Simulations of both linear and radial growth at strong and weak cell-cell adhesion strengths in the presence of quenched

TABLE I. The parameters for the cells used in this paper. These values are based on the HeLa (named after Henrietta Lacks [56]) cell properties. † indicates units of Δt and $*$ units of mean time to cell division, which varies between cell types and is set to 1.0 in CELLSIM3D.

Parameter	Notation	Simulation units	SI units	
Nodes per cell	N_c	180		
Node mass	m	0.04	40	fg
Bond stiffness	k^B	1000	100	nN/μm
Bond damping coefficient	γ_{int}	100	0.01	g/s
Minimum pressure	$(PS)_0$	50	0.5	nN/μm^2
Maximum pressure	$(PS)_\infty$	65	0.65	nN/μm^2
Pressure growth rate	$\Delta(PS)$	0.002	2.0×10^{-5}	nN/μm^2
Attraction stiffness	K^A	10–2000	1–200	nN/μm
Strong attraction stiffness	K^A_{strong}	2000	200	nN/μm
Weak attraction stiffness	K^A_{weak}	10	1	nN/μm
Attraction range	R^A_0	0.3	3	μm
Repulsion stiffness	K^R	10×10^5	10×10^4	nN/μm
Repulsion range	R^A_0	0.2	2	μm
Growth count interval		1000	†	
Intermembrane friction	γ_{ext}	1	10	μg/s
Medium friction	γ_m	0.4	4	μg/s
Time step	Δt	1.0×10^{-4}	$*$	
Threshold division volume	V^{div}	2.9	2900	μm^3

disorder were performed at both low and high disorder densities, see Table I for parameters and Table II for disorder area densities. The initial configuration of the linear interface was a line of 240 cells in a box of size $600 \times 1,000 \times 1.8$. For linear interfaces in the low disorder density regime at weak and strong cell-cell adhesion, 60 000 and 18 000 immobile cells were initially distributed at random inside the box, while in the high-disorder density regime at weak cell-cell adhesion, 72 000 immobile cells were randomly distributed inside the box; see Table II for disorder area density. Figure 1 shows the time evolution of a linear interface.

For radial growth, the initial configuration consisted of a single cell at the center of a box of size $800 \times 800 \times 1.8$. In the low disorder density regime at weak and strong cell-cell adhesion strengths, respectively, 51 200 and 4800 immobile cells were initially distributed at random inside the box. In the case of high disorder density at weak cell-cell adhesion strength, the box contained 77 400 randomly distributed immobile cells; see Table II. In the low disorder density regime, the colonies maintained their circular morphology with interface overhangs. In the high disorder density regime, however, the cell colonies developed a chiral morphology with branched structures lacking circular interfaces for scaling analysis. Snapshots of circular colony expansion, interface evolution, and chiral colony morphology at different times are shown in Fig. 2. Due to cell division and cell migration towards empty spaces, voids become filled over time, see Figs. S2–S6 and the videos [48]. At weak cell-cell adhesion strengths, cells diffuse easily and fill the voids, whereas at high adhesion strengths, cells remain attached to their neighbors after cell division and move collectively to fill the voids. This issue was studied in detail in our previous work, and the results and morphologies are in excellent agreement with experiments [52].

TABLE II. The area density, $\frac{N}{A}$, for quenched disorder in SI units ($\frac{1}{\mu m^2}$) in the different configurations (linear and radial), and at different attraction stiffnesses ($\frac{nN}{\mu m}$). The parameters for the strong and weak cases are given in Table I.

Configuration \ Attraction stiffness	1 (weak)	200 (strong)
Moving linear interface	0.0010	0.0003
Moving linear interface at high disorder density	0.0012	
Moving radial interface	0.0008	0.000075
Pinned radial interface	0.0012	

III. ANALYSES

A. Scaling analysis

1. Interface width

The standard deviation of the front height across a length scale l at time t can be used to define the interface's local width function, $w(l,t)$, which represents the fluctuation around the average height of the interface [57] as

$$w(l,t) = \left\{ \frac{1}{N} \sum_{i=1}^{N} [h_i(t) - \langle h_i \rangle_l]^2 \right\}_L^{\frac{1}{2}}, \tag{3}$$

where L is the the length of the growing front. For radial growth, the height, $h_i(t)$, is replaced by the distance $r_i(t)$ from the center of mass of the cell colony. $\langle h_i \rangle_l$ is the local average over windows of arc length l, and $\{.\}_L$ is the overall average [10,32]. The fluctuations cannot increase indefinitely, and there exists a saturation time, t_s, that depends on the window size [10,26]. For $t \ll t_s$, the value of the local width function $w(l,t)$ increases with time as

$$w(l,t) \sim t^\beta \text{ for } t \ll t_s, \tag{4}$$

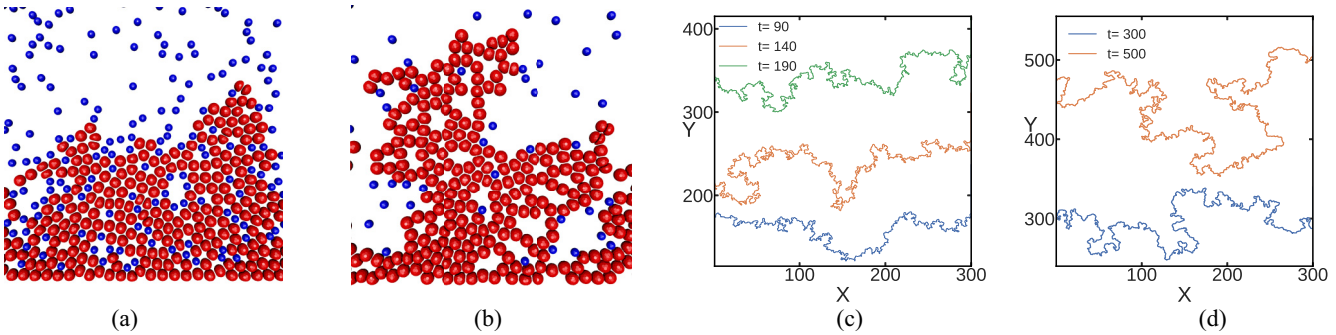

(a) (b) (c) (d)

FIG. 1. (a), (b) Colony expansion (red cells) in a medium with quenched disorder (blue cells) with linear initial configuration. (a) At weak and (b) strong cell-cell adhesion strength. (c), (d) Interface evolution at different times (c) at weak and (d) strong cell-cell adhesion strength. The scaling analysis was done using overhang-corrected interfaces [57]. For units, see Table I.

where β is the growth exponent. For times greater than the saturation time $t \gg t_s$, when the local length l equals the total interface length L, the width function $w(L,t)$ represents the interface variance and increases with the interface length L according to $w(L,t) \sim L^{\alpha}$, where α is to referred to as the global roughness exponent [57].

However, for $t > t_s$ the local width function $w(l,t)$ increases as a function of the local length, l, with a local roughness exponent [57] $\alpha_{\rm loc}$ as

$$w(l,t) \sim l^{\alpha_{\rm loc}}. \tag{5}$$

The local roughness exponent may differ from the global roughness exponent and can also be derived from the power-law behavior of the height-height correlation function, which is defined as

$$C(\ell,t) = \langle |h(x,t) - h(x+\ell,t)|^2 \rangle_x \sim \ell^{2\zeta} \text{ for } \ell \ll \xi_{\parallel}, \tag{6}$$

where $\xi_{\parallel}$ is the parallel correlation length of the interface, and ℓ is the lateral distance between different points on the interface [57–59]. For self-affine interfaces, the height-height correlation function, $C(\ell,t)$, obeys the Family-Vicsek scaling ansatz [60]

$$C(\ell,t) \sim \ell^{2\zeta} c(\ell/t^{1/z^c}), \tag{7}$$

where $c(x)$ is constant for $x \ll 1$ and $c(x) \sim x^{-2\zeta}$, for $x \gg 1$. In growth models with anomalous behavior, the global roughness (α) and dynamic exponents (z) calculated from the interface width function differ from ζ and z^c calculated from the height-height correlation function [58,61]. In these models, the scaling function $c(x)$ can be different from constant for $x \ll 1$, and the scaling relation for the height-height correlation function becomes [58,59]

$$C(\ell,t) \sim C(1,t)\ell^{2\zeta} c(\ell/\xi(t)), \tag{8}$$

where $\xi(t) = [t/C(1,t)]^{1/z^c}$. The average step height, $C(1,t)$, grows as

$$C(1,t) \sim t^{2\lambda}. \tag{9}$$

This modified scaling ansatz, Eq. (8), implies $\alpha = \zeta + \lambda z/2(1-\lambda)$ and $z = z^c/(1-\lambda)$ [59].

2. *Structure factor*

The above real-space analysis takes into account all wavelengths, including short ones, which indicates that finite-size effects can be expected. As a solution, the power-law behavior of the power spectrum of the height fluctuations where only long-wavelength modes contribute to the scaling behavior should be analyzed [62,63]. To calculate the structure factor,

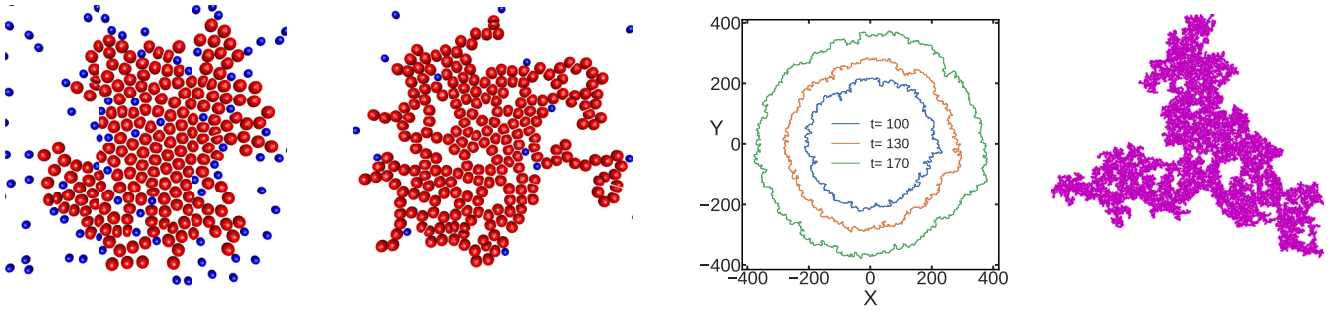

(a) (b) (c) (d)

FIG. 2. (a), (b) Radially growing colonies (red cells) in a medium with quenched disorder (blue cells). (a) At weak and (b) strong cell-cell adhesion strength. (c) Interface evolution at different times at weak cell-cell adhesion strength. The interface has overhangs, but the scaling analysis was done using overhang-corrected interfaces [57]. (d) The morphology for a system started with a single cell at the center of a box on a substrate with a high density of quenched disorder at weak cell-cell adhesion strength. Due to the high disorder density, the morphology is not round but instead chiral with branched structures. Eventually, the interface becomes pinned by the disorder and the growth stops. The final population of the cell colony consists of roughly 10 000 cells. For units, see Table I.

$S(k,t) = \langle \hat{h}(k,t)\hat{h}(-k,t)\rangle$, the kth Fourier mode $\hat{h}(k,t)$ needs to be evaluated [57].

The Family-Vicsek scaling form of the structure factor can be then given as

$$S(k,t) = k^{-(2\alpha+1)} s(kt^{\frac{1}{z}}), \quad \text{where} \tag{10}$$

$$s(u = kt^{\frac{1}{z}}) = \begin{cases} \text{const} & \text{for } u \gg 1 \\ u^{2\alpha+1} & \text{for } u \ll 1. \end{cases} \tag{11}$$

Here, α is the global roughness exponent and $s(u = kt^{\frac{1}{z}})$ the scaling function. Systems with different local and global roughness exponents represent what is known as anomalous roughening [64]. This phenomenon has been observed in various growth models [65–67] and experiments [26,68,69]. Two known types of anomalous roughening are intrinsic anomalous roughening, where $\alpha_{\text{loc}} < 1$ and $\alpha > \alpha_{\text{loc}}$, and superroughening, where $\alpha > 1$ and $\alpha_{\text{loc}} = 1$ [64,70]. In such systems the scaling function, $s(u)$, has the general form

$$s(u = kt^{\frac{1}{z}}) = \begin{cases} u^{2(\alpha-\alpha_s)} & \text{for } u \gg 1 \\ u^{2\alpha+1} & \text{for } u \ll 1, \end{cases} \tag{12}$$

where the spectral roughness exponent, α_s, is independent from the global roughness exponent. In systems with intrinsic anomalous roughening, $\alpha_s = \alpha_{\text{loc}} < 1$, and α_s is different from the global roughness exponent, α.

B. Chi-squared minimization

Chi-squared minimization was used to determine the slope and the y intercept of the line that best fits the data. As every data point in our case was measured ten times, there is a standard error σ_i that can be associated with the individual points in the graphs at different times or lengths. The model's prediction is a lin-lin or log-log straight line $f(x) = b + a\,x$ with parameters a and b. The Chi-squared function is calculated by summing the squares of the differences between the model's prediction and the observed data y_i, then dividing by the data's variance. It is defined as

$$\tilde{\chi}^2 = \sum_{i=1}^{N_d} \frac{(y_i - f(x_i; a, b))^2}{\sigma_i^2}, \tag{13}$$

where N_d is the total number of data points. The optimal values for the model parameters a and b are obtained by minimization of the chi-squared function. Goodness of fit, the p-values, are calculated from the chi-squared probability function $Q(\chi^2|N_d - 2)$ corresponding to the probability of accepting the null hypothesis of obtaining the same model parameters if the experiment were performed numerous times with identical setup. A p value near unity indicates that the fit is good, whereas a small p value indicates that the fit is poor.

IV. RESULTS

A. Interface velocity

For both linear and radial colonies at low disorder densities, the interfaces move at a constant velocity and do not become pinned by disorder, Fig. 3. When cell-cell adhesion is weak, cells are able to detach from their neighbors and diffuse more easily than when cell-cell adhesion is strong. Therefore, cells can move to a location with more space to grow and divide faster due to less contact forces from neighboring cells, resulting in a higher cell proliferation rate and a higher interface velocity (see also the Supplemental Material videos [48]).

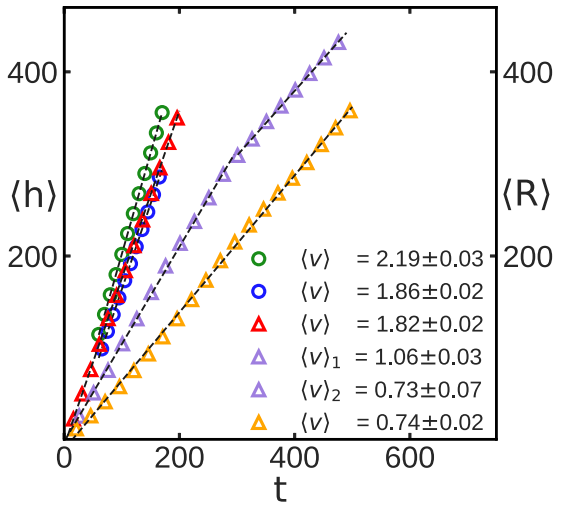

FIG. 3. Interface velocity calculated from the time evolution of the mean colony radius ($\langle R\rangle$) and the mean interface height ($\langle h\rangle$) for radially expanding interfaces (circles) (1) at weak (green circles) and (2) at strong (blue circles) adhesion strength. Correspondingly, for the linearly expanding interfaces (triangles) (1) at weak (red triangles) (2) at strong (orange triangles) adhesion strength at low disorder density, and (3) at weak adhesion strength at high disorder density (purple triangles). For units, see Table I.

In the case of linear interface at weak cell-cell adhesion strength, the interface moves at the velocity of $\langle v\rangle = 1.82 \pm 0.02$. At strong cell-cell adhesion strength, the velocity drops to $\langle v\rangle = 0.74 \pm 0.02$.

In radial interface growth, the velocities are higher, $\langle v\rangle = 2.19 \pm 0.03$ at weak cell-cell adhesion strength, and $\langle v\rangle = 1.86 \pm 0.02$ in the case of strong adhesion strength.

Two cases deserve special attention: First, in linear growth with weak cell-cell adhesion and high disorder density, the growth slows down and there is a crossover from $\langle v\rangle_1 = 1.06 \pm 0.03$ at short times to $\langle v\rangle_2 = 0.73 \pm 0.07$ at late times. Second, in the case of weak adhesion strength and high disorder density in circular expansion, the colonies develop a chiral morphology in which the branches proliferate and get pinned over time, preventing the definition of a circular interface and the evaluation of its velocity.

B. Fractal dimension

The fractal dimensions of the interfaces were evaluated using the box-counting method, Fig. 4. As a general trend, the fractal dimensions of the linear interfaces are slightly larger compared to the circular ones. In addition, the fractal dimensions here are slightly higher than those in the absence of quenched disorder [17]. Table III lists the fractal dimensions in the current paper, and several past experiments and simulations under different conditions.

The one outlier regarding the fractal dimension is the system that develops chiral morphology, that is, the

TABLE III. Interface fractal dimension (d_f), global (α), and local (α_{loc}) roughness exponents, correlation function exponent [ζ; Eq. (6)], growth exponent (β), and average step height exponent (λ), in different configurations with different cell-cell adhesion stiffness strengths, and quenched disorder densities, see Tables I and II. For the DLA-like chiral geometry, the fractal dimension is the colony fractal dimension. The exponents for the well-known cases of KPZ, qKPZ, and MBE for one-dimensional interfaces are also given for reference. † indicates experiments in heterogeneous media and ∗ indicates the crossover with two different regimes.

Configuration	Adhesion	d_f	α	α_{loc}	ζ	β	λ
Kardar-Parisi-Zhang (KPZ) [30]			1/2	1/2		1/3	
quenched KPZ (qKPZ) [31]			3/4	3/4		3/5	
Molecular beam epitaxy (MBE) [61]			3/2	1.0		3/8	
linear interface at high disorder density	weak	1.33 ± 0.06	0.50 ± 0.03	0.53 ± 0.05	0.53 ± 0.01	0.49 ± 0.07	
linear interface at low disorder density	weak	1.34 ± 0.03	0.52 ± 0.04	0.53 ± 0.02	0.53 ± 0.01	0.33 ± 0.08	
linear interface	strong	1.28 ± 0.07	0.47 ± 0.07	0.55 ± 0.05	0.53 ± 0.01	0.67 ± 0.07	
circular interface at high disorder density	weak	1.74 ± 0.06					
DLAlike chiral geometry							
circular interface at low disorder density	weak	1.23 ± 0.02	0.64 ± 0.04	0.60 ± 0.02	0.58 ± 0.01	0.46 ± 0.13	
circular interface	strong	1.23 ± 0.01	0.63 ± 0.04	0.62 ± 0.02	0.58 ± 0.01	0.47 ± 0.13	
Mazarei *et al.* [17] (linear interface)	weak	1.22 ± 0.01	0.75 ± 0.04	0.59 ± 0.01	$0.51 \pm 0.01^*$ $0.31 \pm 0.03^*$	0.28 ± 0.01	0.02 ± 0.01
Mazarei *et al.* [17] (linear interface)	strong	1.26 ± 0.01	0.52 ± 0.02	0.62 ± 0.02	$0.55 \pm 0.01^*$ $0.33 \pm 0.04^*$	0.25 ± 0.02	0.01 ± 0.01
Mazarei *et al.* [17] (circular interface)	weak	1.13 ± 0.01	0.95 ± 0.04	0.66 ± 0.01	$0.59 \pm 0.01^*$ $0.32 \pm 0.01^*$	0.40 ± 0.04	0.37 ± 0.01
Mazarei *et al.* [17] (circular interface)	strong	1.21 ± 0.01	0.71 ± 0.02	0.70 ± 0.01	$0.60 \pm 0.01^*$ $0.35 \pm 0.01^*$	0.42 ± 0.06	0.47 ± 0.01
Bru *et al.* [10] (circular interface)		$1.12 - 1.34 \pm 0.03$	1.5 ± 0.15	0.90 ± 0.10		0.38 ± 0.07	
Huergo *et al.* [29] (circular & Vero Cells)		1.20 ± 0.05	0.5 ± 0.05			0.32 ± 0.04	
Huergo *et al.* [32] (circular & HeLa Cells)		1.20 ± 0.05	0.5 ± 0.05			0.32 ± 0.04	
Huergo *et al.*† [5] (linear & Vero Cells)			0.63 ± 0.03			0.75 ± 0.05	
Vicsek *et al.*† [33] (linear interface)			0.78 ± 0.07				
Galeano *et al.*† [7] (circular interface)		1.18 ± 0.02	0.86 ± 0.04				
Rapin *et al.*† [6] (linear interface)					0.58^* $0.13 - 0.25^*$		

circularly growing system with high disorder density. The result is $d_f = 1.74 \pm 0.06$. This value is within the margin of error to computer simulations of the diffusion limited aggregation (DLA) fractal model with $d_f^{DLA} = 1.71$ [71,72]. This chiral morphology has no well-defined interface but rather a branched structure, and it has been observed, for example, in bacterial growth on agar plates with a low nutrient concentration [73–75].

C. Roughness exponents for linear interfaces

The interface roughness, $w(l,t)$, was evaluated from Eq. (4). For linear interface growth with quenched disorder, increasing the cell-cell adhesion strength or the disorder density resulted in higher growth exponents (β) than in the absence of disorder, see Ref. [17] and Table III. The local roughness exponents, α_{loc}, were obtained from Eq. (5). The exponents have the same value at weak adhesion strength for both low and high disorder density. At strong adhesion strength and low disorder density, α_{loc} increases slightly, Table III. These local roughness exponents are also less than what has been obtained from simulations without quenched disorder, see Ref. [17] and Table III.

The global roughness exponents (α) were calculated via structure factor analysis, Eq. (11). The results are shown in Fig. 5. As in the case of α_{loc}, the global roughness exponents have lower values than those from simulations without quenched disorder [17]; see Table III. The values are in the same range and independent of the adhesion strength and disorder concentration, whereas for linear colony growth in media without quenched disorder [17], the value of the global roughness exponent depends on the adhesion strength, see Table III.

Figure 6 shows the correlation exponent (ζ) defined via Eq. (6). Interestingly, the exponent is the same in all cases for linear growth, independent of the disorder density or cell-cell adhesion, Table III. The scaling regime, however, increases as cell-cell adhesion increases.

The correlation exponent was also determined in the absence of disorder based on the data from Ref. [17]. In that case, the correlation function shows a crossover between two exponents both at weak and strong cell-cell adhesion, Table III. For shorter scales, the exponents are within the error margin of the value $\zeta^{weak} = 0.53$ obtained in the presence of disorder. For longer scales, the exponent crosses over to about $\zeta \approx 0.32$.

The scaling exponents of linear interface growth at low disorder density and at weak adhesion strengths are compatible with KPZ scaling exponents, whereas the global roughness exponent of linear interface growth at weak adhesion strengths in media without quenched disorder is greater than the KPZ global roughness exponent;, see Table III.

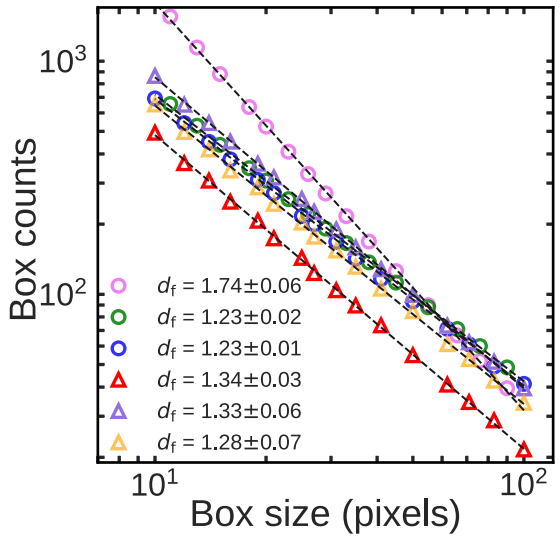

FIG. 4. Fractal dimension (d_f) determined by plotting box counts versus box size for the linear interface (triangles) (1) at weak (red triangles), (2) at strong (orange triangles) adhesion strength, and (3) at weak cell-cell adhesion in high disorder density (purple triangle). Correspondingly, for the radially expanding interface (circles), (1) at weak (green circles), (2) at strong (blue circles) cell-cell adhesion, and high disorder density (violet circles). The colony fractal dimension, (d_f^{col}), for colony expansion at weak cell-cell adhesion began with a single cell in the center of a box on a substrate with a high density of quenched disorder. This system does not have a dense and round morphology, instead it forms slowly to a chiral morphology with branched structure until the colony interface becomes pinned to the disorder on the substrate. The colony fractal dimension is very close to the DLA fractal model, $d_f = 1.71$.

D. Roughness exponents for radial growth

Next, we determine the scaling exponents for radially expanding interfaces. As for linear interfaces, the presence of disorder leads to higher growth exponents (β) compared to the cases with no disorder, Table III. Similarly to linear colony growth, the local roughness exponents (α_{loc}) are in the same range, but somewhat smaller than without disorder [17], see Table III.

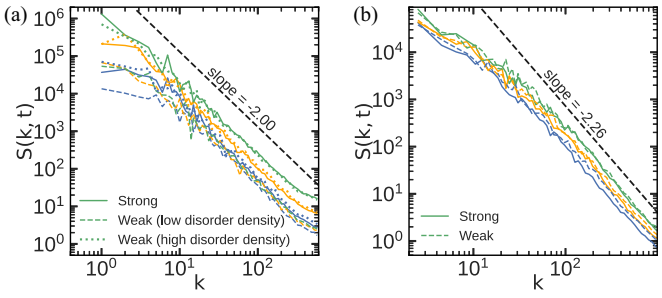

FIG. 5. The structure factor [Eq. (10)] measured at three different times, green: Long time; orange: Intermediate time; blue: Short time, and different conditions (indicated by line type; legend). (a) For the linear interface: Solid lines: Strong cell-cell adhesion and low disorder density; dashed lines: Weak adhesion, low disorder density; dotted lines: Weak adhesion, high disorder density. The black dashed line with a slope of $= -2.0$ is drawn to guide the eye. (b) For the radial interface at low disorder density: Solid lines: Strong cell-cell adhesion; dashed lines: Weak adhesion. The black dashed line with a slope of $= -2.26$ is drawn to guide the eye. The global roughening exponent for each case is reported in Table III. For units, see Table I.

The global roughness exponents (α) were calculated via structure factor analysis, Eq. (11). Similar to linearly expanding interfaces, for the radially expanding interfaces in media with quenched disorder, the global roughness exponents are in the same range and independent of the adhesion strengths, where, as previously mentioned, the global roughness exponent depends on the adhesion strength in the absence of quenched disorder, see Fig. 5 and Table III.

The global roughness exponents in media with quenched disorder, similar to linearly expanding interfaces, are smaller than the global roughness exponents for the radially expanding interface in media without quenched disorder [17], see Table III.

The correlation exponents (ζ) were obtained by determining the height-height correlation function, Eq. (6), shown in Fig. 6, and they have the same value at both strong and weak adhesion strengths, see Table III. Figure 6 shows the height-height correlation functions for radially expanding interfaces in media without quenched disorder and show a crossover with two different correlation exponents for both weak and strong cell-cell adhesion, see Table III.

V. DISCUSSION AND CONCLUSIONS

Comparison of the present data with previous results for epithelial tissue growth in media without quenched disorder [17] shows that quenched disorder can significantly alter the morphology of the interface and cell colony. It also affects cell motility and duplication rate in the colony, resulting in higher fractal dimensions and slower spreading rates. This is consistent with previous experiments for cell colony growth in plain and gel media [5,76].

Our simulations show that at the limit of high disorder concentration, colony growth exhibits branched chiral morphologies and the fractal dimension is close to the fractal dimension of clusters in DLA [71]. This has also been observed in bacterial growth on agar plates at low nutrient concentrations [73–75]. In the absence of quenched disorder, increasing adhesion strength affects the colony morphology and increases the interface fractal dimension [17]. Here, we have shown that the fractal dimension is independent of the cell-cell adhesion strength for colony expansion on heterogeneous substrates for the range of interactions considered.

We studied the roughness exponents which may be used to identify the dominant growth mechanisms, such as surface diffusion and lateral growth, which affect the roughness of a surface and influence how tumors grow and spread. It is, however, important to keep in mind that the exponents here and in other out-of-equilibrium phenomena are dynamic critical exponents and hence they do not have the same universality as the exponents in critical phenomena.

In the absence of disorder, adhesion strength is a crucial parameter that generates both KPZ and MBE-like scaling for colony expansion at strong and weak cell-cell adhesion strengths, respectively [17]. This indicates that for tumor growth at strong cell-cell adhesion, it is more difficult for the cells to separate from their neighbors, and they adhere to one

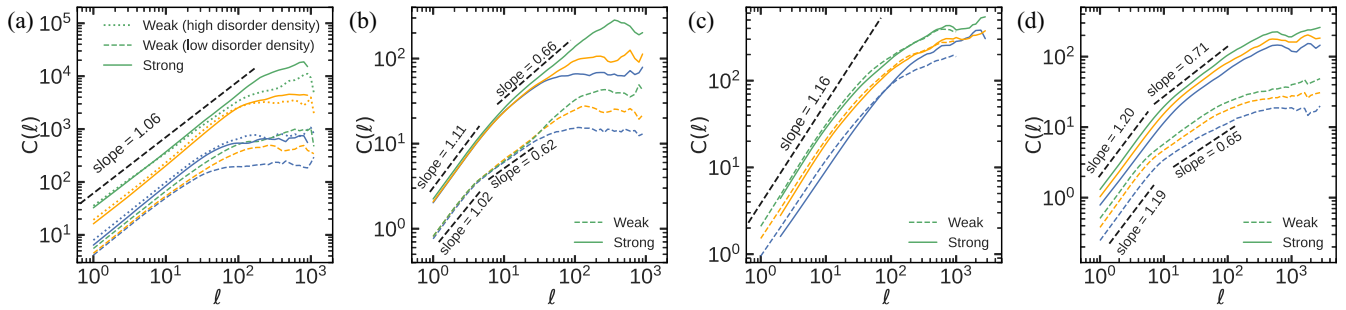

FIG. 6. The height-height correlation function versus length (ℓ) for the linear interface in a medium (a) with quenched disorder, (b) without quenched disorder, and for the radial interface in a medium, (c) with quenched disorder, and (d) without quenched disorder at (green) long, (orange) intermediate, and (blue) short time at different adhesion strengths and disorder densities. Solid lines: Strong cell-cell adhesion and low disorder density; dashed lines: Weak adhesion, low disorder density; dotted lines: Weak adhesion, high disorder density. The correlation function exponents, ζ, are reported in Table III. For units, see Table I.

another after division, thereby making diffusion at the colony interface more difficult. In such a situation, the main growth mechanism at the tumor surface is lateral growth [28,29,32]. In contrast, at weak cell-cell adhesion strength, it is easier for cells to detach and diffuse at the colony interface, see Fig. S6, and the main growth mechanism at the tumor surface is cell diffusion [10,26].

The presence of disorder changes the above. Here, we have demonstrated that in the presence of quenched disorder, the local and global roughness exponent are independent of adhesion strength. This indicates that the effect of adhesion strength on interface roughness and morphology become less significant on heterogeneous substrates which is likely in *in vivo* situations due to factors including, e.g., the extracellular matrix and nutrient concentration. Roughness exponent close to 0.5 at both weak and strong adhesion strengths demonstrates that quenched disorder decreases cell diffusion at the interface colony and generates rougher interfaces.

Disorder does, however, alter the growth exponent. The growth exponent for linear colony expansion at strong adhesion obtained here is within the margin of error of the experimental results of Huergo *et al.* for linear interface expansion of Vero cells in a gel medium [5]. However, in the case of linear interface expansion at weak adhesion with both high and low disorder, the growth exponent is different from the one reported by Huergo *et al.*

At low disorder density and weak adhesion, colony expansion from a single line showed KPZ-like scaling. This is in contrast to the situation without disorder [17]. Although increasing adhesion strength and disorder density does not affect the local and global roughness exponents, the higher disorder density leads to higher growth exponents and makes the scaling behavior of this configuration unclassified. The systems with radial growth at both weak and strong adhesion in media with low disorder density do not show any scaling universality class behavior. This is in contrast to the case of weak adhesion strength in the absence of disorder that displays MBE-like behavior [17].

The distinction between the roughness exponents in the absence and presence of quenched disorder highlights the fact that *in vitro* and *in vivo* tumor growth follows distinct dynamics. *In vitro* and in the absence of quenched disorder, growth dynamics and morphology are sensitive to the cells' mechanical properties, whereas *in vivo*, growth dynamics (under heterogeneous conditions) appears being less responsive to the cells' mechanical properties such as the cell-cell adhesion strength. These results indicate that the concepts of scaling behavior in characterizing cell colony growth should be used with caution due to the sensitivity to parameters such as disorder concentration and cell-cell adhesion strengths.

The growth exponents for linear and radial interface growths differ for both strong and weak cell-cell adhesion. The fractal dimensions for radial interfaces are lower than the fractal dimensions for linear interfaces, and the local and global roughness exponents are greater for the radial interface than for the linear interface. The substrate topologies for linear and radial colony expansions are different. The radial configuration grows on a plane, whereas the linear configuration grows on a cylinder because of the periodicity in one direction. Both the plane and the cylinder have the same Gaussian curvature. However, the first homotopy groups of a plane and a cylinder are different, despite the fact that there is no local difference between the two. A continuous contraction to a point is possible for every closed loop in the plane, but only for some closed loops on the cylinder.

Independent of adhesion strength and the geometries studied here, interface growth in media without quenched disorder does not belong to the superroughening or the intrinsic anomalous roughness subclasses reported in Refs. [26,64–66,68,70]. The average step height exponent, λ, and the modified scaling ansatz for the height-height correlation function [Eq. (8)] [58,59], are also not applicable to the type of anomalous behavior in interface growth in media without quenched disorder. The results imply the existence of another type of anomalous behavior, perhaps necessitating a diferent scaling ansatz for the interface width scaling relation.

ACKNOWLEDGMENTS

M.K. thanks the Discovery and Canada Research Chairs Programs of the Natural Sciences and Engineering Research Council of Canada (NSERC) for financial support. M.M. thanks Western University's Science International Engagement Fund (SIEF) for travel support. Computational resources were provided by the Finnish Grid and Cloud Infrastructure FGCI, funded by the Academy of Finland, Grant No. 304973.

[1] A. Pathak and S. Kumar, Independent regulation of tumor cell migration by matrix stiffness and confinement, Proc. Natl. Acad. Sci. USA **109**, 10334 (2012).

[2] V. Gkretsi and T. Stylianopoulos, Cell adhesion and matrix stiffness: Coordinating cancer cell invasion and metastasis, Front. Oncol. **8**, 145 (2018).

[3] H. K. Kleinman, D. Philp, and M. P. Hoffman, Role of the extracellular matrix in morphogenesis, Curr. Opin. Biotechnol. **14**, 526 (2003).

[4] C. Frantz, K. M. Stewart, and V. M. Weaver, The extracellular matrix at a glance, J. Cell Sci. **123**, 4195 (2010).

[5] M. A. C. Huergo, N. E. Muzzio, M. A. Pasquale, P. H. Pedro González, A. E. Bolzán, and A. J. Arvia, Dynamic scaling analysis of two-dimensional cell colony fronts in a gel medium: A biological system approaching a quenched Kardar-Parisi-Zhang universality, Phys. Rev. E **90**, 022706 (2014).

[6] G. Rapin, N. Caballero, I. Gaponenko, B. Ziegler, A. Rawleigh, E. Moriggi, T. Giamarchi, S. A. Brown, and P. Paruch, Roughness and dynamics of proliferating cell fronts as a probe of cell–cell interactions, Sci. Rep. **11**, 8869 (2021).

[7] J. Galeano, J. Buceta, K. Juarez, B. Pumarino, J. De La Torre, and J. Iriondo, Dynamical scaling analysis of plant callus growth, Europhys. Lett. **63**, 83 (2003).

[8] I. Pastushenko, A. Brisebarre, A. Sifrim, M. Fioramonti, T. Revenco, S. Boumahdi, A. Van Keymeulen, D. Brown, V. Moers, S. Lemaire, S. De Clercq, E. Minguijón, C. Balsat, Y. Sokolow, C. Dubois, F. De Cock, S. Scozzaro, F. Sopena, A. Lanas, N. D'Haene *et al.*, Identification of the tumour transition states occurring during EMT, Nature (London) **556**, 463 (2018).

[9] S. SenGupta, C. A. Parent, and J. E. Bear, The principles of directed cell migration, Nat. Rev. Mol. Cell Biol. **22**, 529 (2021).

[10] A. Brú, S. Albertos, J. Luis Subiza, J. L. García-Asenjo, and I. Brú, The universal dynamics of tumor growth, Biophys. J. **85**, 2948 (2003).

[11] J. Pérez-Beteta, D. Molina-García, J. A. Ortiz-Alhambra, A. Fernández-Romero, B. Luque, E. Arregui, M. Calvo, J. M. Borrás, B. Meléndez, A. Rodriguez de Lope *et al.*, Tumor surface regularity at mr imaging predicts survival and response to surgery in patients with glioblastoma, Radiology **288**, 218 (2018).

[12] J. Pérez-Beteta, D. Molina-García, A. Martínez-González, A. Henares-Molina, M. Amo-Salas, B. Luque, E. Arregui, M. Calvo, J. M. Borrás, J. Martino *et al.*, Morphological MRI-based features provide pretreatment survival prediction in glioblastoma, Eur. Radiol. **29**, 1968 (2019).

[13] A. Buttenschön and L. Edelstein-Keshet, Bridging from single to collective cell migration: A review of models and links to experiments, PLoS Comput. Biol. **16**, e1008411 (2020).

[14] I. M. Wortel and J. Textor, Artistoo, a library to build, share, and explore simulations of cells and tissues in the web browser, Elife **10**, e61288 (2021).

[15] R. Conradin, C. Coreixas, J. Latt, and B. Chopard, PalaCell2D: A framework for detailed tissue morphogenesis, J. Comput. Sci. **53**, 101353 (2021).

[16] J. Li, S. K. Schnyder, M. S. Turner, and R. Yamamoto, Role of the cell cycle in collective cell dynamics, Phys. Rev. X **11**, 031025 (2021).

[17] M. Mazarei, J. Åström, J. Westerholm, and M. Karttunen, *In silico* testing of the universality of epithelial tissue growth, Phys. Rev. E **106**, L062402 (2022).

[18] A. Larkin and Y. N. Ovchinnikov, Pinning in type II superconductors, J. Low Temp. Phys. **34**, 409 (1979).

[19] L. Balents and M. P. A. Fisher, Temporal order in dirty driven periodic media, Phys. Rev. Lett. **75**, 4270 (1995).

[20] M. Karttunen, M. Haataja, K. R. Elder, and M. Grant, Defects, order, and hysteresis in driven charge-density waves, Phys. Rev. Lett. **83**, 3518 (1999).

[21] J. P. Bouchaud, E. Bouchaud, G. Lapasset, and J. Planès, Models of fractal cracks, Phys. Rev. Lett. **71**, 2240 (1993).

[22] D. S. Fisher, Threshold behavior of charge-density waves pinned by impurities, Phys. Rev. Lett. **50**, 1486 (1983).

[23] F. Costa, M. Campos, and M. da Silva, The universal growth rate behavior and regime transition in adherent cell colonies, J. Theor. Biol. **387**, 181 (2015).

[24] E. Khain and J. Straetmans, Dynamics of an expanding cell monolayer, J. Stat. Phys. **184**, 20 (2021).

[25] M. Radszuweit, M. Block, J. G. Hengstler, E. Schöll, and D. Drasdo, Comparing the growth kinetics of cell populations in two and three dimensions, Phys. Rev. E **79**, 051907 (2009).

[26] A. Brú, J. M. Pastor, I. Fernaud, I. Brú, S. Melle, and C. Berenguer, Super-rough dynamics on tumor growth, Phys. Rev. Lett. **81**, 4008 (1998).

[27] A. Brú, S. Albertos, J. L. Subiza, J. L. Garcia-Asenjo, and I. Brú, Reply to comments by Buceta and Galeano regarding the article "The universal dynamics of tumor growth," Biophys. J. **88**, 3737 (2005).

[28] M. A. C. Huergo, M. A. Pasquale, A. E. Bolzán, A. J. Arvia, and P. H. González, Morphology and dynamic scaling analysis of cell colonies with linear growth fronts, Phys. Rev. E **82**, 031903 (2010).

[29] M. A. C. Huergo, M. A. Pasquale, P. H. González, A. E. Bolzán, and A. J. Arvia, Dynamics and morphology characteristics of cell colonies with radially spreading growth fronts, Phys. Rev. E **84**, 021917 (2011).

[30] M. Kardar, G. Parisi, and Y.-C. Zhang, Dynamic scaling of growing interfaces, Phys. Rev. Lett. **56**, 889 (1986).

[31] Z. Csahók, K. Honda, E. Somfai, M. Vicsek, and T. Vicsek, Dynamics of surface roughening in disordered media, Physica A **200**, 136 (1993).

[32] M. A. C. Huergo, M. A. Pasquale, P. H. González, A. E. Bolzán, and A. J. Arvia, Growth dynamics of cancer cell colonies and their comparison with noncancerous cells, Phys. Rev. E **85**, 011918 (2012).

[33] T. Vicsek, M. Cserző, and V. K. Horváth, Self-affine growth of bacterial colonies, Physica A **167**, 315 (1990).

[34] S. N. Santalla, J. Rodríguez-Laguna, J. P. Abad, I. Marín, M. M. Espinosa, J. Muñoz-García, L. Vázquez, and R. Cuerno, Nonuniversality of front fluctuations for compact colonies of nonmotile bacteria, Phys. Rev. E **98**, 012407 (2018).

[35] S. V. Buldyrev, A.-L. Barabási, F. Caserta, S. Havlin, H. E. Stanley, and T. Vicsek, Anomalous interface roughening in porous media: Experiment and model, Phys. Rev. A **45**, R8313(R) (1992).

[36] K. Sneppen, Self-organized pinning and interface growth in a random medium, Phys. Rev. Lett. **69**, 3539 (1992).

[37] H. Leschhorn, Anisotropic interface depinning: Numerical results, Phys. Rev. E **54**, 1313 (1996).

[38] S. N. Santalla and S. C. Ferreira, Eden model with nonlocal growth rules and kinetic roughening in biological systems, Phys. Rev. E **98**, 022405 (2018).

[39] E. Young, G. Melaugh, and R. J. Allen, Active layer dynamics drives a transition to biofilm fingering, npj Biofilms Microbio. **9**, 17 (2023).

[40] X. Wang, H. A. Stone, and R. Golestanian, Shape of the growing front of biofilms, New J. Phys. **19**, 125007 (2017).

[41] M. Block, E. Schöll, and D. Drasdo, Classifying the expansion kinetics and critical surface dynamics of growing cell populations, Phys. Rev. Lett. **99**, 248101 (2007).

[42] Y. Azimzade, A. A. Saberi, and M. Sahimi, Effect of heterogeneity and spatial correlations on the structure of a tumor invasion front in cellular environments, Phys. Rev. E **100**, 062409 (2019).

[43] J. A. Bonachela, C. D. Nadell, J. B. Xavier, and S. A. Levin, Universality in bacterial colonies, J. Stat. Phys. **144**, 303 (2011).

[44] D. Bi, X. Yang, M. C. Marchetti, and M. L. Manning, Motility-driven glass and jamming transitions in biological tissues, Phys. Rev. X **6**, 021011 (2016).

[45] D. E. P. Pinto, Margarida M. Telo da Gama, and N. A. M. Araújo, Cell motility in confluent tissues induced by substrate disorder, Phys. Rev. Res. **4**, 023186 (2022).

[46] P. Madhikar, J. Åström, J. Westerholm, and M. Karttunen, CellSim3D: GPU accelerated software for simulations of cellular growth and division in three dimensions, Comput. Phys. Commun. **232**, 206 (2018).

[47] Open source software at https://github.com/softsimu/cellsim3d.

[48] See Supplemental Material at http://link.aps.org/supplemental/10.1103/PhysRevE.108.054405 for four videos: (1) linear geometry with weak cell-cell adhesion and disorder, (2) linear geometry with weak cell-cell adhesion without disorder, (3) linear geometry with strong cell-cell adhesion and disorder, and (4) linear geometry with strong cell-cell adhesion without disorder. The cells are shown in blue and disorder, when present, is shown in black. The videos are available for downloading at https://doi.org/10.5281/zenodo.8112841. The supplemental PDF file contains details of the CELLSIM3D model, estimation of the minimal sample size, and additional snapshots of the systems, which also includes Refs. [77–85].

[49] P. Murray, G. Frampton, and P. Nelson, Cell adhesion molecules, BMJ **319**, 332 (1999).

[50] G. M. Edelman and K. L. Crossin, Cell adhesion molecules: Implications for a molecular histology, Annu. Rev. Biochem. **60**, 155 (1991).

[51] M. P. Stewart, J. Helenius, Y. Toyoda, S. P. Ramanathan, D. J. Muller, and A. A. Hyman, Hydrostatic pressure and the actomyosin cortex drive mitotic cell rounding, Nature (London) **469**, 226 (2011).

[52] P. Madhikar, J. Åström, B. Baumeier, and M. Karttunen, Jamming and force distribution in growing epithelial tissue, Phys. Rev. Res. **3**, 023129 (2021).

[53] X. Trepat, M. R. Wasserman, T. E. Angelini, E. Millet, D. A. Weitz, J. P. Butler, and J. J. Fredberg, Physical forces during collective cell migration, Nat. Phys. **5**, 426 (2009).

[54] P. Madhikar, J. Åström, J. Westerholm, B. Baumeier, and M. Karttunen, Coarse-grained modeling of cell division in 3d: Influence of density, medium viscosity, and inter-membrane friction on cell growth and nearest neighbor distribution, Soft Mater. **18**, 150 (2020).

[55] O. Wartlick, P. Mumcu, A. Kicheva, T. Bittig, C. Seum, F. Julicher, and M. Gonzalez-Gaitan, Dynamics of Dpp signaling and proliferation control, Science **331**, 1154 (2011).

[56] W. F. Scherer, J. T. Syverton, and G. O. Gey, Studies on the propagation in vitro of poliomyelitis viruses. IV. Viral multiplication in a stable strain of human malignant epithelial cells (strain HeLa) derived from an epidermoid carcinoma of the cervix, J. Exp. Med. **97**, 695 (1953).

[57] A.-L. Barabási and H. E. Stanley, *Fractal Concepts in Surface Growth* (Cambridge University Press, Cambridge, UK, 1995).

[58] M. Schroeder, M. Siegert, D. Wolf, J. Shore, and M. Plischke, Scaling of growing surfaces with large local slopes, Europhys. Lett. **24**, 563 (1993).

[59] M. Kotrla and P. Šmilauer, Nonuniversality in models of epitaxial growth, Phys. Rev. B **53**, 13777 (1996).

[60] F. Family and T. Vicsek, Scaling of the active zone in the Eden process on percolation networks and the ballistic deposition model, J. Phys. A: Math. Gen. **18**, L75 (1985).

[61] S. Das Sarma, S. V. Ghaisas, and J. M. Kim, Kinetic superroughening and anomalous dynamic scaling in nonequilibrium growth models, Phys. Rev. E **49**, 122 (1994).

[62] D. Liu and M. Plischke, Universality in two-and three-dimensional growth and deposition models, Phys. Rev. B **38**, 4781 (1988).

[63] M. Plischke and Z. Rácz, Dynamic scaling and the surface structure of eden clusters, Phys. Rev. A **32**, 3825 (1985).

[64] J. M. López, M. A. Rodriguez, and R. Cuerno, Superroughening versus intrinsic anomalous scaling of surfaces, Phys. Rev. E **56**, 3993 (1997).

[65] J. Krug, Turbulent interfaces, Phys. Rev. Lett. **72**, 2907 (1994).

[66] J. M. López and M. A. Rodríguez, Lack of self-affinity and anomalous roughening in growth processes, Phys. Rev. E **54**, R2189(R) (1996).

[67] S. Das Sarma, C. J. Lanczycki, R. Kotlyar, and S. V. Ghaisas, Scale invariance and dynamical correlations in growth models of molecular beam epitaxy, Phys. Rev. E **53**, 359 (1996).

[68] H. N. Yang, G. C. Wang, and T. M. Lu, Instability in low-temperature molecular-beam epitaxy growth of Si/Si (111), Phys. Rev. Lett. **73**, 2348 (1994).

[69] J. M. Lopez and J. Schmittbuhl, Anomalous scaling of fracture surfaces, Phys. Rev. E **57**, 6405 (1998).

[70] J. J. Ramasco, J. M. López, and M. A. Rodríguez, Generic dynamic scaling in kinetic roughening, Phys. Rev. Lett. **84**, 2199 (2000).

[71] T. A. Witten and L. M. Sander, Diffusion-limited aggregation, a kinetic critical phenomenon, Phys. Rev. Lett. **47**, 1400 (1981).

[72] P. Meakin, Diffusion-controlled cluster formation in 2–6-dimensional space, Phys. Rev. A **27**, 1495 (1983).

[73] E. Ben-Jacob, O. Shochet, A. Tenenbaum, I. Cohen, A. Czirók, and T. Vicsek, Communication, regulation and control during complex patterning of bacterial colonies, Fractals **02**, 15 (1994).

[74] H. Fujikawa and M. Matsushita, Fractal growth of *Bacillus subtilis* on agar plates, J. Phys. Soc. Jpn. **58**, 3875 (1989).

[75] M. Matsushita and H. Fujikawa, Diffusion-limited growth in bacterial colony formation, Physica A **168**, 498 (1990).

[76] N. E. Muzzio, M. A. Pasquale, M. A. C. Huergo, A. E. Bolzán, P. H. González, and A. J. Arvia, Spatio-temporal morphology changes in and quenching effects on the 2D spreading dynamics of cell colonies in both plain and methylcellulose-containing culture media, J. Biol. Phys. **42**, 477 (2016).

[77] D. A. Fletcher and R. D. Mullins, Cell mechanics and the cytoskeleton, Nature (London) **463**, 485 (2010).

[78] F. van Roy and G. Berx, The cell-cell adhesion molecule E-cadherin, Cell. Mol. Life Sci. **65**, 3756 (2008).
[79] M. P. Stemmler, Cadherins in development and cancer, Mol. BioSyst. **4**, 835 (2008).
[80] C. D. Buckley, G. E. Rainger, P. F. Bradfield, G. B. Nash, and D. L. Simmons, Cell adhesion: More than just glue (Review), Mol. Membr. Biol. **15**, 167 (1998).
[81] M. A. Wozniak, K. Modzelewska, L. Kwong, and P. J. Keely, Focal adhesion regulation of cell behavior, Biochim. Biophys.-Molec. Cell Res. Cell Adhes. Signalling **1692**, 103 (2004).
[82] L. Petruzzelli, M. Takami, and H. D. Humes, Structure and function of cell adhesion molecules, Am. J. Med. **106**, 467 (1999).
[83] A. Mkrtchyan, J. Åström, and M. Karttunen, A new model for cell division and migration with spontaneous topology changes, Soft Matter **10**, 4332 (2014).
[84] J. Huang, J. O. Cochran, S. M. Fielding, M. C. Marchetti, and D. Bi, Shear-driven solidification and nonlinear elasticity in epithelial tissues, Phys. Rev. Lett. **128**, 178001 (2022).
[85] G. Miaoulis and R. D. Michener, *An Introduction to Sampling* (Kendall, Dubuque, Iowa, 1976).